Title

Nonlocal Means Denoising of Self-Gated and k-Space Sorted 4-Dimensional Magnetic Resonance Imaging Using Block-Matching and 3-Dimensional Filtering: Implications for Pancreatic Tumor Registration and Segmentation.

Journal

International journal of radiation oncology, biology, physics, 95(3)

ISSN

0360-3016

Authors

Jin, Jun
McKenzie, Elizabeth
Fan, Zhaoyang
et al.

Publication Date

2016-07-01

DOI

10.1016/j.ijrobp.2016.02.006

Peer reviewed

HHS Public Access

Author manuscript

Int J Radiat Oncol Biol Phys. Author manuscript; available in PMC 2017 July 01.

Published in final edited form as:

Int J Radiat Oncol Biol Phys. 2016 July 1; 95(3): 1058–1066. doi:10.1016/j.ijrobp.2016.02.006.

Non-local means denoising of SG-KS-4D-MRI using block matching 3D: Implications for pancreatic tumor registration and segmentation

Jun Jin, MS[3], **Elizabeth McKenzie, MS**[1], **Zhaoyang Fan, PhD**[2], **Richard Tuli, MD, PhD**[1], **Zixin Deng, MS**[2], **Jianing Pang, PhD**[2], **Benedick Fraass, PhD**[1], **Debiao Li, PhD**[2], **Howard Sandler, MS, MD**[1], **Guang Yang, BS**[3], **Ke Sheng, PhD**[4], **Shuiping Gou, PhD**[3], and **Wensha Yang, PhD**[1,*]

[1]Department of Radiation Oncology, Cedars Sinai Medical Center, Los Angeles 90048

[2]Biomedical Imaging Research Institute, Department of Biomedical Sciences, Cedars Sinai Medical Center, Los Angeles 90048

[3]Department of Computer Science, Xidian University, Xi'An 710071, China

[4]Department of Radiation Oncology, University of California at Los Angeles, 90024

Introduction

Respiration-induced tumor and organ motion poses great challenges in radiation therapy (RT).[1] In conventional RT, a 3D-CT is used to define the tumor volume with a generic margin applied to compensate for the geometric uncertainties of internal organ motion that is not captured by the 3D-CT. The emergence of 4D imaging has enabled the internal organ motion to be individually resolved to allow more accurate tumor motion assessment. As a result, 4D-CT has been established as the current clinical standard for assessing motion. However, there are intrinsic limitations of 4D-CT including poor soft tissue contrast, stitching artifacts and increased radiation dose. These issues are particularly prominent when treating abdominal tumors where 4D-CT has been shown to be unsatisfactory.[2]

Magnetic resonance imaging (MRI) provides superior soft tissue contrast and versatile imaging sequences. Using fast imaging sequences, such as steady state free precession and turbo spin echo, real time 2D images can be obtained for motion assessment.[3] Unlike CT, the 2D-MRI images can be acquired in any orientation including the dominant tumor motion axes, which has prompted ongoing investigation for RT. On the other hand, real time MRI is limited to one to a few slices of 2D images, which are inadequate to capture the complex geometric relationships between the tumor and surrounding critical organs. MRI sequences

*Corresponding author: Wensha Yang, Ph.D, Department of Radiation Oncology, Cedars Sinai Medical Center, 8700 Beverly Blvd. Los Angeles, CA 90048, wensha.yang@cshs.org.

Conflicts of interest: none

based on resorting of 2D images or k-space data have been developed by multiple research groups[4–7]. These methods provide excellent in-plane but poor cross-plane image resolution due to variation in breathing patterns, which lead to stitching artifacts similar to those seen in the 4D-CT. Our team has developed a novel 4D-MRI sequence based on 3D radial acquisition using **s**elf-**g**ating and **k**-space **s**orting (SG-KS-4D-MRI) that provides images with isotropic high resolution and an absence of stitching artifacts.[8] However, SG-KS-4D-MRI images are noisy, which is attributed to three major factors. First, aggressive under-sampling, especially in patients with high incidence of irregular breathing, may result in aliasing artifacts that appear as a nearly uniform background haze.[9] In theory, increasing the image acquisition time would increase the number of valid radial lines which contribute to higher signal to noise ratio (SNR). However, this would incur practical issues such as patient discomfort and low-throughput scanning. Second, large gradient jumps in k-space may cause eddy current effects. Third, 3D volumetric acquisition may lead to inadequate B_0 shimming and more B_0 off-resonance, resulting in more streaking artifacts and noise than 2D acquisition. All the above aspects are believed to contribute to random noise level.

Image post processing is an appealing alternative to enhance the image SNR if imaging details can be preserved. Conventional imaging denoising methods based on smoothing and low-pass filtering tend to lose image details that are important for RT[10]. More advanced filters such as anisotropic diffusion and total variation can improve major edge preservation but still lose fine textures of images heavily contaminated by noise[11]. Compared to the local means method, non-local means methods have been developed to collectively enhance image SNR based on the self-similarity of the image while maximally preserving imaging texture[12]. Among existing non-local means denoising methods, block matching 3D (BM3D) has been used to successfully denoise natural and medical images[13], although the implementation of BM3D has been limited to 2D or 3D images. The purpose of this study is to employ BM3D on SG-KS-4D-MRI images to mitigate random noise and study the effect of BM3D denoising on 4D image registration and segmentation for pancreatic cancer patients. Potentially the same algorithm can be implemented on other types of 4D images to reduce random noise.

Methods and Materials

Nine patients diagnosed with locally advanced or borderline resectable pancreatic cancer were included in the study under a protocol approved by the IRB. One patient had two synchronous and separate lesions present in the head and tail of the pancreas. The other eight patients had a single lesion present in the head or body of the pancreas.

SG-KS-4D-MRI acquisition

The sequence used in the 4D-MRI has been introduced in detail in our previous publications.[8] In short, a spoiled gradient recalled echo (GRE) sequence with a 3D radial-sampling K-space trajectory and 1D projection-based self-gating was implemented on a 3.0 Tesla system (Magnetom Verio™, Siemens Healthcare, Germany). The data acquisition continued in an 8-minute free-breathing scan (prescribed isotropic spatial resolution=1.6mm, a cubic imaging volume of 300x300x300 mm^3, flip angle=10°, TR/echo time=5.8/2.6ms,

readout band width=399 Hz/pixel). The gating signals were retrospectively extracted for breathing pattern analysis and K-space data resorting.

4D-MRI image denoising

For image denoising we closely follow the method described by Sheng et al[13]. The input 4D-MRI images were first normalized to have an image intensity range of [0, 255].

Step1: Construction of 3D blocks from 4D-MRI patches—Assuming the signals of sub-regions of the same image can be similar but the noise is random, the principle of BM3D is to search for these similar image patches and then collectively enhance the signal while suppressing the noise. Although this method has been primarily used on 2D natural images, it is particularly suited to 4D acquisitions with highly correlated images in both the spatial and temporal domain. Therefore, we modified the original BM3D method to search in the increased spatial and temporal dimensions.

First, an 8×8 pixel patch in the 4D-MRI to be denoised is selected as the reference patch. For clarity, the term slice is used consistently to describe a 2D plane in the 3D image while a frame is used to describe a 2D image in the time series. It is important to note that the similarity measurement is performed in the wavelet transfer domain such that

$$d\left(P_{I_R}, P_I\right) = \|W^{-1}\Gamma W(P_{I_R}) - W^{-1}\Gamma W(P_I)\| \quad (1)$$

Where P_{IR} is the reference patch and P_I is the selected patch for similarity calculation. W and W^{-1} are forward and inverse wavelet transformations. Γ is a hard threshold to suppress excessive image noise before calculating the patch distance initially. In our study the result was not sensitive to Γ, which was subsequently set to 1. A 3D stack is created following the order of similarity to the reference patch (as shown in Figure 1) after searching the original slice *and* four of its adjacent slices and frames. The collection of patches for the reference patch is then denoted as:

$$C_{I_R} = \left\{ I \in X_{ij} : d(P_{I_R}, P_I) \leq \tau \right\} \quad (2)$$

where i and j denote the coordinates of the image patches within the i^{th} 2D slice and j^{th} frame of the 4D MRI. d is the similarity measurement between the reference patch P_{IR} and the matching patch P_I, and τ is another hard threshold selected by the use for the similarity measure d. Individual results may be improved by tuning the denoising threshold (τ), but it would make the method much less practical and applicable. In this study, a single denoised threshold of 15 showed the best average performance, and was applied to all patients. A more stringent threshold would limit the SNR improvement but prevent unintended modification of the images. The use of the 2-norm allows evaluation of the distance in the Wavelet domain without inverse transfer due to the conservation of energy such that:

$$d(P_{I_R}, P_I) = \|W(P_{I_R}) - W(P_I)\|_2^2 \quad (3)$$

To reduce computational cost and assume a greater similarity between patches proximal to each other, the search window is limited to the four temporal frames and spatial slices adjacent to the reference slice for a total of nine 2D images included in the search.

Step 2: Collaborative denoising—Once the noisy patch set is constructed, a group denoising is performed in 3D space. Since a 2D patch in the 3D block member for a reference imaging patch can also be the member of another reference patch, resultant denoised imaging patches were aggregated to give greater weights to denoised patches from less noisy groups. A second denoising step was performed to restore more details and improve the overall BM3D performance as described previously.

Bior1.5 wavelets were used in the 2D transform in both steps 1 and 2 following previous publications[14, 15]. A normalized 1D discrete cosine transform (DCT) was used in the 3rd dimension for 3D transformations.

For comparison, anisotropic diffusion (AD) [16] was used for edge preserving denoising of the 4D-MRI. This is achieved by adding an edge-stopping function in the classical diffusion equation such that:

$$\frac{\partial X(\vec{x}, t)}{\partial t} = div(g(\|\nabla X\|)\nabla X) \quad (4)$$

$$g\|\nabla X\| = \exp(-\frac{\|\nabla X\|^2}{2t^2}) \quad (5)$$

In our simulation, t was set at 100 with three iterations performed.

4D-MRI image registration, segmentation, volume and noise analysis

Pancreatic gross tumor volume (GTV) was contoured on the first end-of-exhalation phase of the 4D-MRI by a single radiation oncologist. The same volume was used as a starting volume before 4D image registration. A B-spline based deformable registration was performed on both the raw and denoised 4D-MRI images using VelocityAI™ (Varian, Palo Alto). The GTV was then propagated to other phases based on the 4D deformable registration.

As shown in figure 2, the noise is defined using coefficient of variance (CoV) calculated from a volume of interest (VOI) with diameter of 5mm. The VOI was placed in an approximately featureless region of the normal liver to minimize the uncertainties in the noise calculation. The contrast to noise ratio (CNR) is defined as absolute intensity

difference between artery in the liver and the surrounding liver tissue divided by the standard deviation of liver tissue, as noted in the equation 6,

$$CNR = \frac{|S_A - S_B|}{\sigma_B} \quad (6)$$

in which S_A is the average intensity (signal) in the artery, S_B is the average signal in the surrounding liver tissue, and σ_B is the standard deviation in the surrounding liver tissue. Imaging intensity profiles were also created to inspect the fluctuation of the intensities across tumor volume. [17, 18]

The reproducibility of the tumor position at end-of-exhalation (EOE) was evaluated by the difference in the tumor center of mass locations for each patient, $d_{EOE} = |EOE2 - EOE1|$ as shown in figure 2c, in three cardinal planes. The standard deviation (σ_GTV) of the GTVs was calculated from ten phases for both the raw and the denoised 4D-MRI images. A paired t test was used to compare the difference between the parameters calculated on the raw 4D-MRI vs. the denoised 4D-MRI image sets. A p value ≤ 0.05 was considered statistically significant. In order to analyze the consistency of the tumor volume trajectory after applying BM3D, a two dimensional cross-correlation (CC) was calculated comparing vector trajectories extracted from the raw and denoised 4D-MRI using the corr2 function in Matlab (MathWorks, Natick, MA).

Results

The BM3D was successfully implemented to denoise all patients' 4D-MRI images. It took 30s to denoise a 4D-MRI set on an i7 core computer and the time can be substantially reduced using a graphic processing unit. The percentage of lines discarded in the k-space data varied among patients between 20% to 40%. Figure 3 shows three example patients, each representing a characteristic respiratory pattern based on the self-gating signals. Figure 3a and b show the raw and denoised images for patients with regular breathing and baseline drifting, respectively. For these two patients, there was only mild loss (20% radial lines were discarded) of radial lines from the original MRI acquisition due to irregular breathing, so the raw 4D-MRI images are relatively free of artifacts and have good soft tissue contrast. However, they are appreciably noisier than a typical breath hold image. BM3D remarkably reduced the random noise without blurring subtle boundaries between structures. Figure 3c represents a patient with an irregular breathing pattern, for which 37% of radial lines were discarded during 4D-MRI reconstruction. As a result, the raw 4D-MRI image showed significant amount of noise throughout the entire acquisition volume and visible streaking artifacts. The distribution of artifacts is consistent with the 3D radial acquisition, which has lower sampling density in outer k-space than in center k-space causing streaking artifacts outside bright areas. Figure 3d shows the intensity profiles from the patient in figure 3b. In this plot, line profiles were calculated along the center of mass of the GTV at three cardinal angles on both the raw and the denoised 4D-MRI. The profiles show that random fluctuations are suppressed in the denoised images while preserving the fine structures. This

feature helps to keep the contrast between GTV and the surrounding soft tissue consistent but also enhances the structured artifacts.

Figure 4 shows the comparison of BM3D to the local denoising method AD. AD with a low diffusion coefficient moderately suppressed the noise. To achieve a similar noise level to that achieved with BM3D, a high diffusion coefficient or more iterations have to be applied, resulting in blurry images that lose low contrast imaging features. In comparison, BM3D was able to effectively suppress the noise and enhance the boundaries between low-contrast structures.

Table 1 shows the summary of all patients. All parameters studied are statistically significantly different using a paired t test to compare raw and denoised groups. The GTV standard deviation (σ_GTV) calculated from ten phases for each patient is statistically lower on the denoised 4D-MRI, with 0.6cc vs. 0.8cc for the denoised and raw groups respectively. The discrepancies in the end of exhalation phase are consistently larger for the raw 4D-MRI. On average the noise is reduced from 7.9% to 3.8% (52% reduction) comparing the raw to denoised 4D-MRI. CNR is also improved from 4.1 to 6.4 (56% enhancement) when comparing the raw and denoised 4D-MRI. The cross correlation comparing tumor trajectories derived from the raw and denoised 4D-MRI is 0.9994±0.0003 (average±stdev).

Discussion

SG-KS-4D-MRI has shown great promise in assessing respiratory motion for abdominal tumors and organs. The 3D radial sampling sequence design has enabled high isotropic resolution, which could not have been achieved with 2D sampling.[19] However, irregularities in patients' breathing patterns, eddy currents resulting from rapid jumping between radial lines, and more sparse sampling density can still lead to noise in the resulting 4D-MRI images. Unlike 2D-sampling based 4D-MRI, which typically shows stitching artifacts between the scan positions, SG-KS-4D-MRI based on 3D radial sampling typically shows both random noise distributed in the entire image acquisition volume and aliasing artifacts that are more conspicuous towards the edge of the imaging volume. In this study, we investigated the effectiveness of post-imaging processing to improve 4D-MRI image quality. Different denoising methods include local means denoising and non-local means denoising. Local means denoising uses the mean value of pixels adjacent to the target pixel to increase SNR, examples including anisotropic diffusion, total variation, and wavelet denoising.[20] Our study shows that anisotropic diffusion cannot reduce noise while preserving the imaging texture that is important for deformable registration and delineation. Non-local means denoising methods use mean values of distant pixels to enhance SNR based on the similarity to the target pixel [21, 22]. One of the non-local means denoising methods, BM3D, has shown great promise to mitigate noise while preserving texture features on natural 2D images and MVCT images, and was chosen for study here. Compared to other imaging techniques, 4D-MRI is particularly suited for the non-local means denoising methods due to the large amount of redundant information presented in adjacent spatial and temporal images, resulting in the qualitative and quantitative image quality improvement shown in this study. In contrast, to achieve the same level of noise reduction from prolonging image acquisition time by acquiring more lines (assuming all noise is random) the total imaging time would

have to be quadrupled, which can be impractical. Moreover, increasing time alone does not eliminate error sources including eddy currents.

Our studies have shown that the novel implementation of BM3D on 4D-MRI images results in significant reduction of imaging noise and improvement of contrast to noise ratio, without modifying the original tumor motion trajectory. The reduction of tumor volume variation is small (0.8cc vs. 0.6cc), but statistically significant; however, the clinical relevance of less tumor volume variation needs to be studied in a larger cohort of patients. The dosimetry of the radiotherapy plans for pancreatic cancer patients is often limited by the serial organ doses in the tumor vicinity, so any reduction on the tumor margin without compromising dose coverage is preferred in this difficult disease site. Hence, there is a strong clinical need in accurate tumor volume assessment during respiration and this study contributes to this clinical need.

It should be pointed out the BM3D algorithm is suited to suppress random noise, but tends to enhance structured artifacts. As shown in figure 5, the structured aliasing artifact in the raw image was enhanced in the denoised image. These patterned artifacts can be mitigated by methods including independent components analysis.[23] Their impact is typically small due to their distal locations to the image center, where the region of interest usually lies. There has been a general concern regarding BM3D, as well as other non-local means denoising methods, that they could modify the original images, but the possibility is minimized using stringent similarity thresholds when building the block (such as were used this study). As a final check, any newly identified feature in the denoised image should be compared against the original noisy image for visual confirmation. Alternatively, iterative MR reconstruction algorithms based on self-consistency can be used. The reconstruction problem can be formulated as an optimization problem with the fidelity term in the k-space and the BM3D regularization applied in the image domain, although the iterative reconstruction can take substantially longer time.

Conclusions

SG-KS-4D-MRI images were post-processed using a non-local means denoising method, block matching 3D (BM3D), with an extended search range in the 3D space domain and 4D time domain. This work shows that BM3D can significantly reduce random noise while maintaining structural features in the SG-KS-4D-MRI datasets. In this study of pancreatic target volume imaging, automatic segmentation of GTV in the registered image sets is shown to be more consistent on the denoised 4D-MRI than on the raw 4D-MRI.

Acknowledgments

This work is supported in part by NCI grant 1R03CA173273

References

1. Gierga DP, Chen GT, Kung JH, Betke M, Lombardi J, Willett CG. Quantification of respiration-induced abdominal tumor motion and its impact on IMRT dose distributions. Int J Radiat Oncol Biol Phys. 2004; 58:1584–1595. [PubMed: 15050340]

2. Ge J, Santanam L, Noel C, Parikh PJ. Planning 4-dimensional computed tomography (4DCT) cannot adequately represent daily intrafractional motion of abdominal tumors. Int J Radiat Oncol Biol Phys. 2013; 85:999–1005. [PubMed: 23102840]

3. Tseng CL, Sussman MS, Atenafu EG, et al. Magnetic resonance imaging assessment of spinal cord and cauda equina motion in supine patients with spinal metastases planned for spine stereotactic body radiation therapy. Int J Radiat Oncol Biol Phys. 2015; 91:995–1002. [PubMed: 25832691]

4. Cai J, Chang Z, Wang Z, Paul Segars W, Yin FF. Four-dimensional magnetic resonance imaging (4D-MRI) using image-based respiratory surrogate: a feasibility study. Med Phys. 2011; 38:6384–6394. [PubMed: 22149822]

5. Tryggestad E, Flammang A, Han-Oh S, et al. Respiration-based sorting of dynamic MRI to derive representative 4D-MRI for radiotherapy planning. Med Phys. 2013; 40:051909. [PubMed: 23635279]

6. Stemkens B, Tijssen RH, de Senneville BD, et al. Optimizing 4-Dimensional Magnetic Resonance Imaging Data Sampling for Respiratory Motion Analysis of Pancreatic Tumors. Int J Radiat Oncol Biol Phys. 2015

7. Hu Y, Caruthers SD, Low DA, Parikh PJ, Mutic S. Respiratory amplitude guided 4-dimensional magnetic resonance imaging. Int J Radiat Oncol Biol Phys. 2013; 86:198–204. [PubMed: 23414769]

8. Deng Z, Pang J, Yang W, et al. Four-dimensional MRI using three-dimensional radial sampling with respiratory self-gating to characterize temporal phase-resolved respiratory motion in the abdomen. Magn Reson Med. 2015

9. Bernstein, MA.; King, KF.; Zhou, X. Handbook of MRI Pulse Sequences. Amsterdam ; Boston: Academic Press; 2004.

10. Cheng H, Huang F. Magnetic resonance imaging image intensity correction with extrapolation and adaptive smoothing. Magn Reson Med. 2006; 55:959–966. [PubMed: 16526014]

11. Gavgani AM, Dogrusoz YS. Noise reduction using anisotropic diffusion filter in inverse electrocardiology. Conf Proc IEEE Eng Med Biol Soc. 2012; 2012:5919–5922. [PubMed: 23367276]

12. Manjón JV, Coupé P, Buades A. MRI noise estimation and denoising using non-local PCA. Med Image Anal. 2015; 22:35–47. [PubMed: 25725303]

13. Sheng K, Gou S, Wu J, Qi SX. Denoised and texture enhanced MVCT to improve soft tissue conspicuity. Med Phys. 2014; 41:101916. [PubMed: 25281968]

14. Dabov K, Foi A, Katkovnik V, Egiazarian K. Image denoising by sparse 3-D transform-domain collaborative filtering. Ieee T Image Process. 2007; 16:2080–2095.

15. Lebrun M. An Analysis and Implementation of the BM3D Image Denoising Method. Imaging Processing On Line. 2012

16. Lu W, Olivera GH, Chen Q, et al. Deformable registration of the planning image (kVCT) and the daily images (MVCT) for adaptive radiation therapy. Phys Med Biol. 2006; 51:4357–4374. [PubMed: 16912386]

17. Alexander ME, Baumgartner R, Summers AR, et al. A wavelet-based method for improving signal-to-noise ratio and contrast in MR images. Magn Reson Imaging. 2000; 18:169–180. [PubMed: 10722977]

18. Reeder SB, Wintersperger BJ, Dietrich O, et al. Practical approaches to the evaluation of signal-to-noise ratio performance with parallel imaging: application with cardiac imaging and a 32-channel cardiac coil. Magn Reson Med. 2005; 54:748–754. [PubMed: 16088885]

19. Yang W, Fan Z, Tuli R, et al. Four-dimensional Magnetic Resonance Imaging with 3D Radial Sampling and Self-gating based K-space Sorting: Early Clinical Experience on Pancreatic Cancer Patients. Vol published on line as article in-press. International Journal of Radiation Oncology Biology Physics. 2015

20. Xing XX, Zhou YL, Adelstein JS, Zuo XN. PDE-based spatial smoothing: a practical demonstration of impacts on MRI brain extraction, tissue segmentation and registration. Magn Reson Imaging. 2011; 29:731–738. [PubMed: 21531104]

21. Lu K, He N, Li L. Nonlocal means-based denoising for medical images. Comput Math Methods Med. 2012; 2012:438617. [PubMed: 22454694]

22. Liu H, Yang C, Pan N, Song E, Green R. Denoising 3D MR images by the enhanced non-local means filter for Rician noise. Magn Reson Imaging. 2010; 28:1485–1496. [PubMed: 20850239]
23. Martel AL, Chan RW, Ramsay E, Plewes DB. Removing undersampling artifacts in DCE-MRI studies using independent components analysis. Magn Reson Med. 2008; 59:874–884. [PubMed: 18302238]

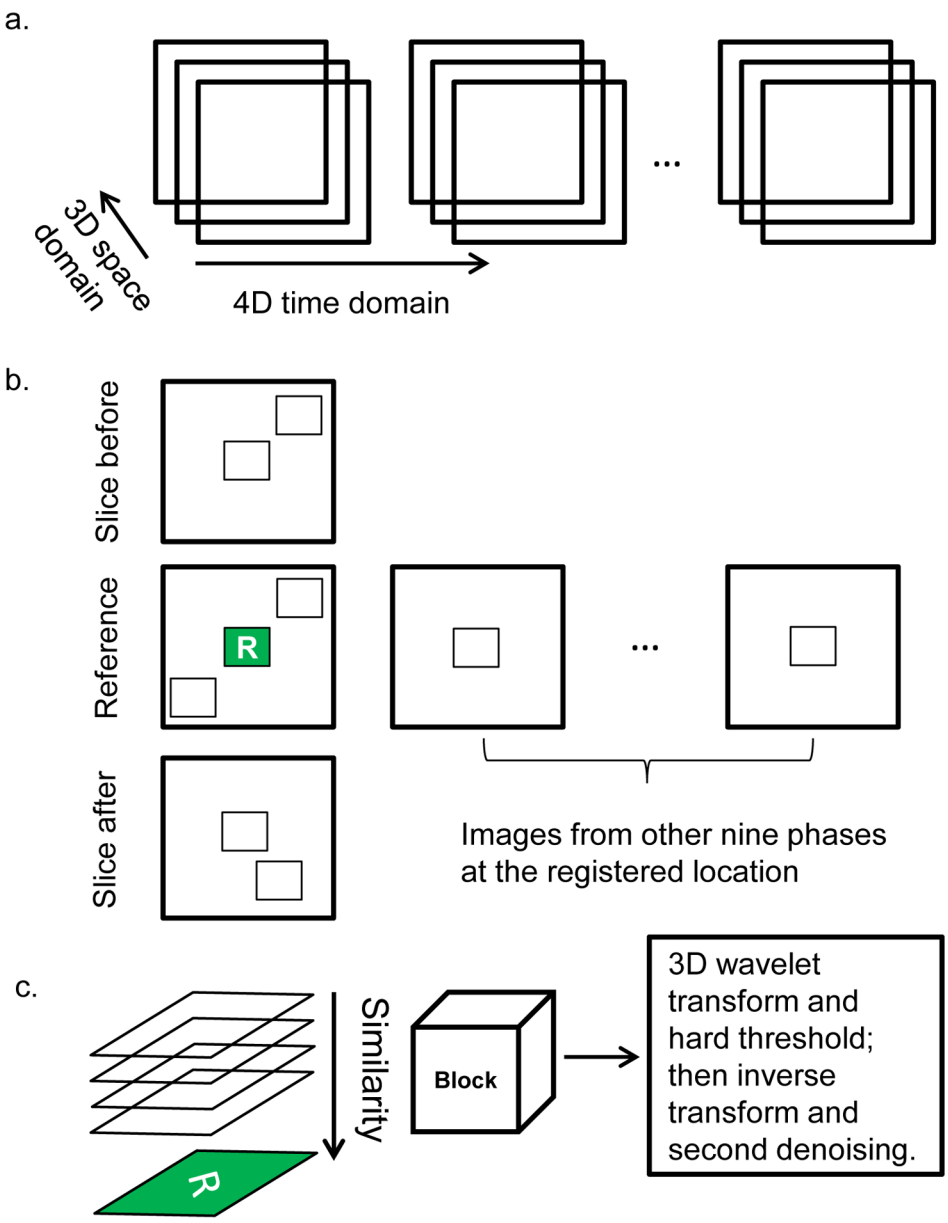

Figure 1.

Schematic representation of applying BM3D to 4D-MRI images in three steps

a. Schematic representation of 4D-MRI images in the 3D space domain and 4D time domain.

b. Patches from the reference image, as well as from the image slices superior and inferior to the reference image, and image slices at the same anatomic location from other breathing phases are searched.

c. Patches were stacked based on the similarity to the reference patch to form a 3D block. 3D wavelet transformation and a hard threshold were applied. Inverse wavelet transformation and second denoising were then performed.

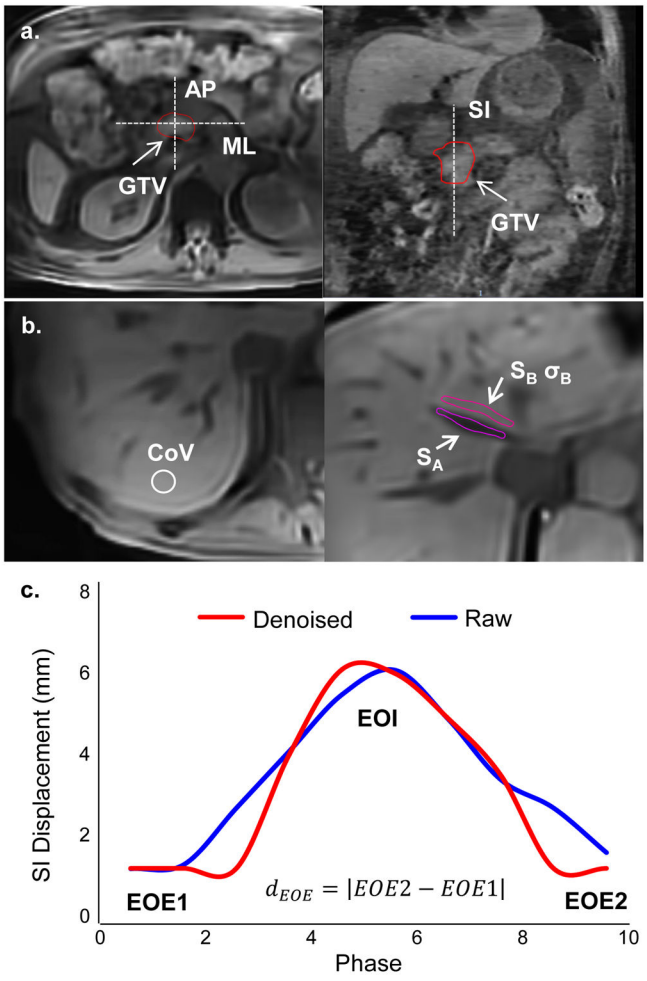

Figure 2.

Images showing the areas that were used to calculate noise (represented by CoV), intensity profiles and CNR.

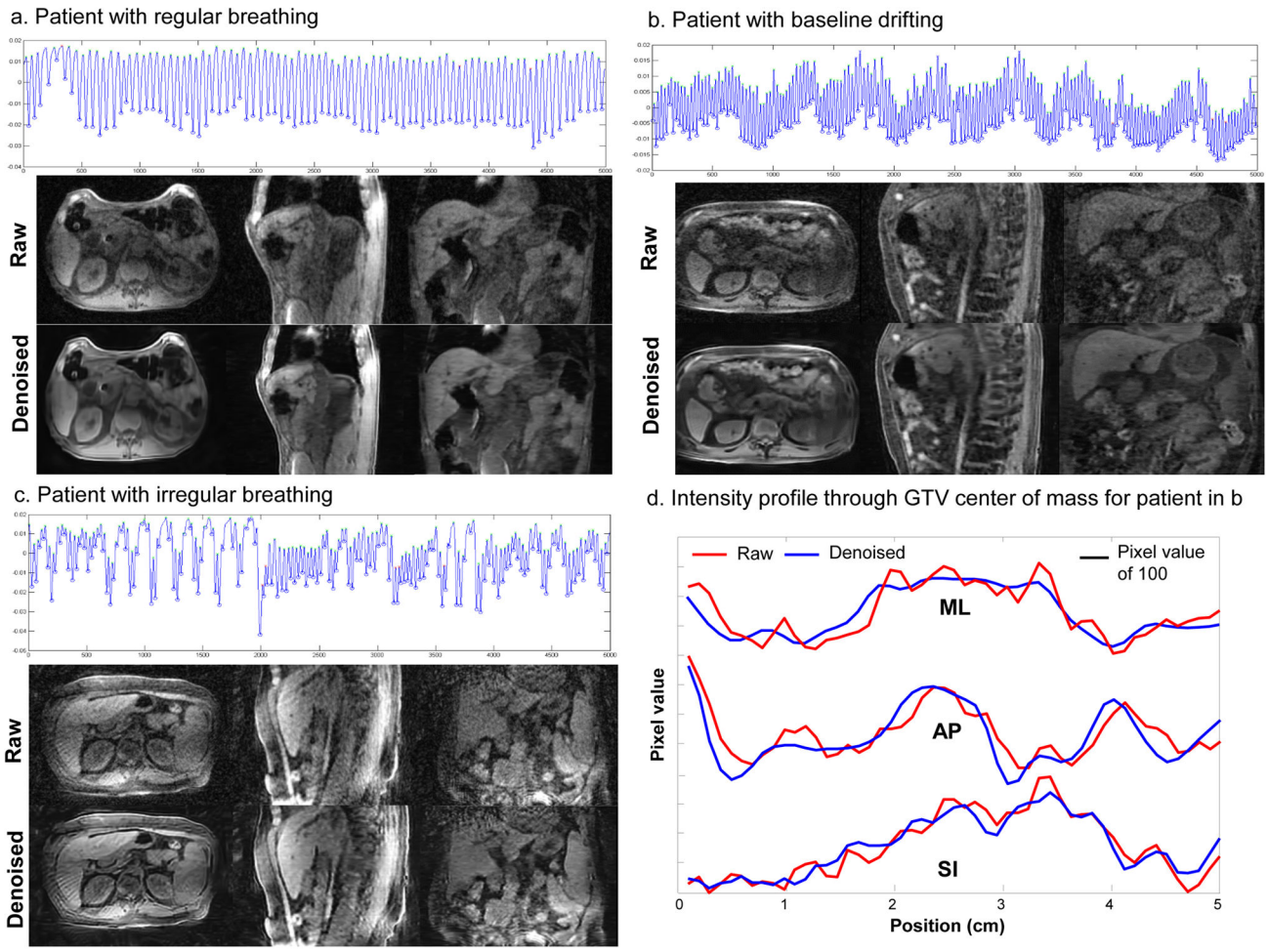

Figure 3.

Raw and denoised 4D-MRI for patients with regular breathing (a), baseline drifting (b), or irregular breathing(c) patterns. Intensity profiles (d) across the center of the GTV for the patient in 3b.

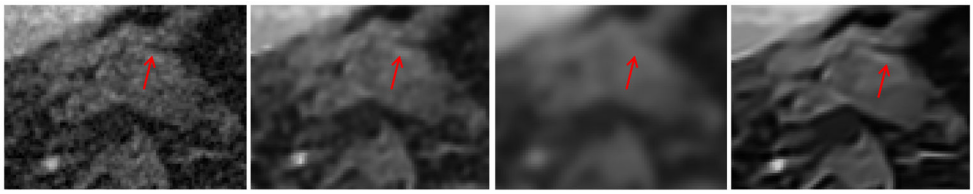

Figure 4.

Comparison of BM3D to two examples of a local means denoising method. a) raw image, b) and c) anisotropic diffusion with low and high diffusion coefficients, respectively, and d) BM3D which shows superior denoising while maintaining structural features.

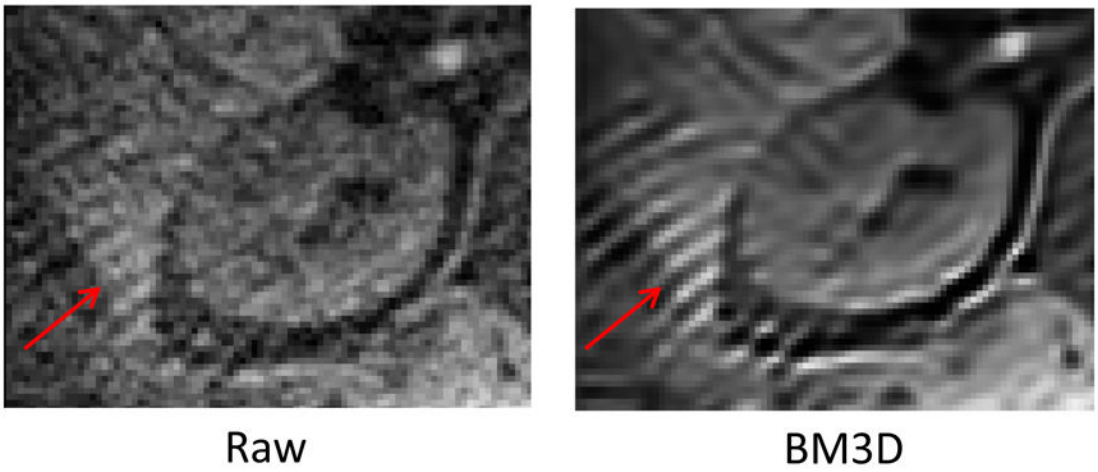

Figure 5.
An example of enhancement in an artifact appearing repetitively at one location by BM3D

Table 1

Patient ID	σ_GTV (cc) Raw/DeN	d_{EOE} (mm) Raw/DeN			CoV (%) Raw/DeN	CNR Raw/DeN	CC (Raw vs. DeN)
		SI	AP	ML			
1a	0.7 / 0.3	1.1 / 0	1.2 / 0	0.3 / 0	7.7 / 2.9	3.2 / 5.6	0.9995
1b	0.6 / 0.4	0.7 / 0	1.5 / 0	0.6 / 0	na	na	0.9996
2	1.7 / 1.2	0.4 / 0	1.3 / 0	0.9 / 0	6.3 / 2.7	5.4 / 5.3	0.9992
3	0.7 / 0.7	0.2 / 0.3	0.7 / 1.2	0.2 / 1.2	5.1 / 4.2	4.6 / 7.4	0.9999
4	0.4 / 0.1	0 / 0	0.1 / 0	0.1 / 0	6.3 / 3.3	4.3 / 4.8	0.9989
5	1.7 / 1.0	0.3 / 0	0.1 / 0	1 / 0	7.6 / 3.7	4.8 / 8.5	0.9991
6	1.3 / 1.0	0.3 / 0	0.8 / 0	0.7 / 0	11.7 / 6.1	2.9 / 5.4	0.9996
7	0.2 / 0.3	0.2 / 0.7	1.1 / 0	0.2 / 0	11.9 / 4.1	4.9 / 9.1	0.9992
8	0.1 / 0.1	1.5 / 1.5	0.3 / 0	0.7 / 0	7.4 / 3.7	3.6 / 5.7	0.9997
9	0.8 / 0.8	0.6 / 0	0.1 / 0	0.7 / 0	7.2 / 3.2	3.3 / 5.6	0.9989
Average	0.8 / 0.6	0.5 / 0.3	0.7 / 0.1	0.5 / 0.1	7.9 / 3.8	4.1 / 6.4	0.9994
Stdev	0.6 / 0.4	0.5 / 0.5	0.5 / 0.4	0.3 / 0.4	2.4 / 1.0	0.9 / 1.6	0.0003
p	0.010 *	0.04 *	0.01 *	0.02 *	0.0001 *	0.0006 *	na

Abbreviations: μ_GTV=average GTV calculated from 10 phases; σ_GTV=standard deviation of GTV calculated from 10 phases; d_{EOE}=absolute difference in tumor locations between the two exhalation phases; CoV=coefficient of variance representing noise; CNR=contrast to noise ratio calculated for the artery in liver; deN=denoised; CC=correlation coefficient;

*statistically significant difference.